

# An Antimony Selenide Molecular Ink for Flexible Broadband Photodetectors

Md Rezaul Hasan, Ebuka S. Arinze, Arunima K. Singh, Vladimir P. Oleshko, Shiqi Guo, Asha Rani, Yan Cheng, Irina Kalish, Mona E. Zaghoul, Mulpuri V. Rao, Nhan V. Nguyen, Abhishek Motayed, Albert V. Davydov, Susanna M. Thon,\* and Ratan Debnath\*

As digital imaging devices gain in popularity, the quest for new infrared-sensitive materials that do not depend on epitaxial thin-film deposition techniques has intensified. The ability to deposit semiconducting films from solution has shown great potential for various electronic and optoelectronic applications and emerged as an attractive low-cost approach to fabricating high-quality semiconducting thin films.<sup>[1–7]</sup> One can simply employ “soft” nonvacuum processes such as spin-coating,<sup>[6,8–11]</sup> ink-jet printing,<sup>[4,12]</sup> and similar techniques to enable high-throughput device fabrication and realize new technologies particularly in the area of flexible optoelectronics.<sup>[11,13,14]</sup>

Research on solution-processed semiconductors has focused on both organic and inorganic systems.<sup>[1,4,5]</sup> However, molecular organic systems have several disadvantages including poor environmental, mechanical, and thermal stability as well as poor electronic transport as compared to their inorganic counterparts. On the other hand, inorganic semiconductors can take advantage of covalently bonded frameworks to achieve desirable electronic transport properties and band gaps.<sup>[15–17]</sup>

There have been tremendous efforts to deposit inorganic films with excellent properties using chemical bath deposition,<sup>[18–21]</sup> spray pyrolysis,<sup>[22,23]</sup> and other solution-based methods.

Among various inorganic semiconductors, metal chalcogenides, particularly, group V–VI compounds have been widely studied for their optoelectrical<sup>[24,25]</sup> and thermoelectric properties<sup>[26,27]</sup> and successfully utilized in thin film transistors,<sup>[5,6]</sup> solar cells,<sup>[7,24,28]</sup> thermoelectric devices,<sup>[29,30]</sup> photodetectors (PDs),<sup>[31–33]</sup> and phase change memory<sup>[34]</sup> applications. These films have typically been prepared via sophisticated deposition techniques such as catalyst-assisted chemical vapor deposition,<sup>[35]</sup> sputtering,<sup>[36]</sup> thermal evaporation,<sup>[24,37]</sup> and molecular beam epitaxy<sup>[38]</sup> that require energy-intensive, high vacuum deposition conditions not amenable to high-throughput mass production.

Although most metal chalcogenides are very difficult to dissolve in common solvents, recent developments in solution-based chemistry of chalcogenides have overcome this limitation, and homogeneous, high-quality semiconductor films derived from true molecular inks have been grown successfully.<sup>[39]</sup> Typically, an ink is made by dissolving stoichiometric amounts of elemental chalcogens with metal in hydrazine solutions.<sup>[6,40]</sup> Unfortunately, hydrazine is highly toxic and explosive, which limits the practicality of production. Some less hazardous and volatile solvents, such as mixtures of amine and thiols, have been used for solution deposition, but their application has been limited to bulk metal chalcogenide thin film growth from their respective compounds.<sup>[39,41,42]</sup>

Antimony selenide (Sb<sub>2</sub>Se<sub>3</sub>) has emerged from the group V–VI chalcogenides as an excellent candidate for optoelectronics due to its direct band gap of about 1.1 eV<sup>[7]</sup> in the NIR regime and p-type semiconductor behavior. 1D Sb<sub>2</sub>Se<sub>3</sub> nanostructures are of particular interest due to their high surface-to-volume ratio and tunable properties that can be used to enhance the performance of optoelectronic devices. Such NWs have been synthesized in the past using solution-based growth methods,<sup>[32,43,44]</sup> but Sb<sub>2</sub>Se<sub>3</sub>-based devices, (e.g., PDs) have been fabricated mostly on rigid substrates.<sup>[32]</sup> The complicated growth methods based on toxic solvents and limited performance to date have hindered Sb<sub>2</sub>Se<sub>3</sub> from competing with traditional crystalline PD technologies.

Here, we report on a method for template-free, facile, one-step solution-based and in-situ growth of Sb<sub>2</sub>Se<sub>3</sub> nanowires (NWs) on flexible polyimide substrates for fast response and high-performance flexible PDs. Our one-pot synthesis method

M. R. Hasan, Dr. A. K. Singh, Dr. V. P. Oleshko, S. Guo, A. Rani, I. Kalish, Dr. A. Motayed, Dr. A. V. Davydov, Dr. R. Debnath  
Materials Science and Engineering Division  
Material Measurement Laboratory  
National Institute of Standards and Technology  
Gaithersburg, MD 20899, USA  
E-mail: ratan.debnath@nist.gov



M. R. Hasan, Prof. M. V. Rao  
Department of Electrical and Computer Engineering  
George Mason University  
4400 University Drive, Fairfax, VA 22030, USA  
E. S. Arinze, Y. Cheng, Prof. S. M. Thon  
Department of Electrical and Computer Engineering  
Johns Hopkins University  
3400 North Charles Street, Baltimore, MD 21218, USA  
E-mail: susanna.thon@jhu.edu  
S. Guo, A. Rani, Prof. M. E. Zaghoul  
Department of Electrical and Computer Engineering  
The George Washington University  
Washington, DC 20052, USA  
Dr. N. V. Nguyen  
Semiconductor and Dimensional Metrology Division  
Physical Measurement Laboratory  
National Institute of Standards and Technology  
Gaithersburg, MD 20899, USA

DOI: 10.1002/aelm.201600182

is based on a molecular ink prepared by directly mixing elemental antimony and selenium into a solution of ethylenediamine (EDA) and 2-mercaptoethanol (ME).<sup>[42]</sup> This is the first time, to our knowledge, that this facile synthesis method has been used to fabricate Sb<sub>2</sub>Se<sub>3</sub> PDs. Chemical, structural and optical properties of the NWs obtained from this technique are characterized. Sb<sub>2</sub>Se<sub>3</sub> PDs fabricated on flexible substrates exhibit excellent figures of merit, such as a broadband photo-response spanning from the ultraviolet (UV) to near-infrared (NIR) range, fast temporal response, and superior mechanical stability. Previous studies on Sb<sub>2</sub>Se<sub>3</sub>-based flexible PDs have primarily focused on using polyethylene terephthalate (PET).<sup>[44]</sup> However, in this study, we substitute PET for polyimide, a film with a higher glass transition temperature (350 vs 78 °C), superior maximum operating temperature (350 vs 160 °C), and chemical exposure while maintaining excellent performance. Additionally, we demonstrate that the spectral response of our detectors should be tunable by adjusting the nanowire size. Our results indicate that molecular-ink-based flexible, scalable, and tunable systems have the potential to replace conventional broadband and NIR optoelectronic technology.

Our deposition method for Sb<sub>2</sub>Se<sub>3</sub> films is depicted in **Figure 1** and involves the following steps: (i) dissolving elemental Sb with excess Se at a molar ratio of 1:3 in EDA and ME to produce the precursor solutions under magnetic stirring for several days in a nitrogen glove box; (ii) spin-casting the resulting dark orange molecular ink onto polyimide substrates, and (iii) annealing the as-deposited films. The details can be found in the Experimental Section.

We used field-emission scanning electron microscopy (FESEM) to image the Sb<sub>2</sub>Se<sub>3</sub> nanostructures on flexible polyimides after thermal processing at 350 °C in the presence of excess Se, as shown in **Figure 2a**. The FESEM image shows the formation of randomly oriented NWs having a small range of lengths and diameters. The processing temperature and selenium concentration are key fabrication parameters as they dictate the aspect ratio of the nanostructures (Figure S1, Supporting Information), which, in turn, affects the device optical properties. Formation of NWs from the as-deposited films takes place at around 200 °C in the presence of excess selenium; however, when the concentration of Se is lowered (to near the stoichiometric concentration), the films grow instead with a nanograin-like morphology. Compositional mapping by energy-dispersive X-ray spectroscopy (EDXS) shows the distribution of Sb and Se elements in the film (Figure S2, Supporting Information), and one can clearly see the individual

nanostructures in the elemental maps. The EDXS spectrum (Figure S2, Supporting Information) exhibits strong Sb and Se peaks, and there is no discernable sulfur present in the film.

Transmission electron microscopy (TEM) measurements revealed rod-like morphology of 0.1–1.2 μm long Sb<sub>2</sub>Se<sub>3</sub> NWs with diameters ranging from 100 to 300 nm (Figure 2b). The corresponding selected-area diffraction (SAED) pattern (Figure 2b, inset) and phase-contrast high-resolution TEM (HRTEM) images (Figure 2c) indicate that the Sb<sub>2</sub>Se<sub>3</sub> nanostructures are single orthorhombic crystals growing along the <001> direction of the *Pbnm* space group. The SAED pattern of an individual NW indexed as the [430] zone shows a 002 point reflection with 0.20 nm lattice spacing ( $d_{002} = 0.19810$  nm) and a 340 point reflection with 0.23 nm lattice spacing ( $d_{340} = 0.23431$  nm). More detailed analysis of SAED patterns revealed additional splitting of {34l} reflections due to twinning of NWs along the growth direction likely caused by close-packed growth conditions. The latter was supported by examination of corresponding TEM micrographs. The HRTEM image in Figure 2c (left) reveals several families of inter-planar lattice fringes, including large 0.58 nm (020) spacing ( $d_{020} = 0.5885$  nm) parallel to the growth direction, and the inset shows a Fast Fourier Transform (FFT) pattern implying [100] orientation for the Sb<sub>2</sub>Se<sub>3</sub> NW sample area indicated by the red box. The enlarged HRTEM fragment (Figure 2c, right) shows orthogonal 0.19 nm (022) and (0-22) lattice fringes observed in the vicinity of a partially amorphized NW surface.

For more accurate evaluation of the nanoscale elemental composition and the spatial uniformities of the Sb and Se elemental distributions, EDXS-FESEM compositional analyses were corroborated with high spatial resolution EDXS and electron energy-loss spectroscopy (EELS). Analyses of randomly selected NWs from the same sample were performed using a 0.2 nm diameter electron probe in scanning transmission electron microscopy (STEM) mode at 300 kV accelerating voltage (Figures S3 and S4, Supporting Information). Elemental mapping results revealed that Sb and Se were uniformly distributed throughout the analyzed NWs (Figure 2d), and elemental line profiles confirmed the same (Figure S3, Supporting Information). X-ray spectra acquired during line profiling have been further quantified using a Cliff–Lorimer thin film ratio technique with calculated k-factors for the Sb K $\alpha$  and the Se K $\alpha$  peaks, and absorption (mass-thickness) correction as described elsewhere.<sup>[45]</sup> Similarly, EELS spectra (Figure S4, Supporting Information) taken in randomly selected spots on the same sample have been quantified using a thin film ratio technique with

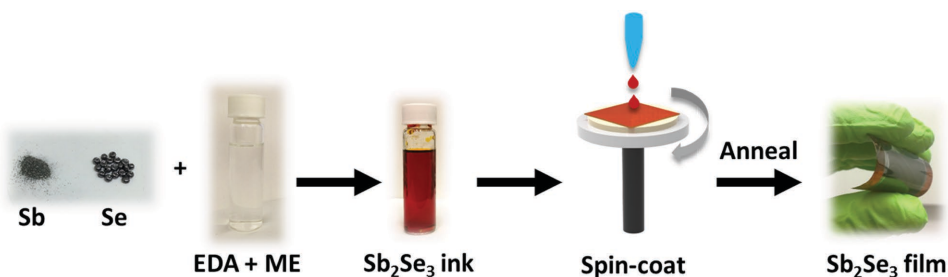


**Figure 1.** Fabrication scheme for Sb<sub>2</sub>Se<sub>3</sub> nanostructure formation on flexible substrates utilizing a molecular ink. The process begins with dissolution of elemental Sb and Se in ethylenediamine (EDA) and 2-mercaptoethanol (ME) to produce a molecular ink that is spin-cast onto a flexible substrate and annealed to form a flexible nanowire-based film.

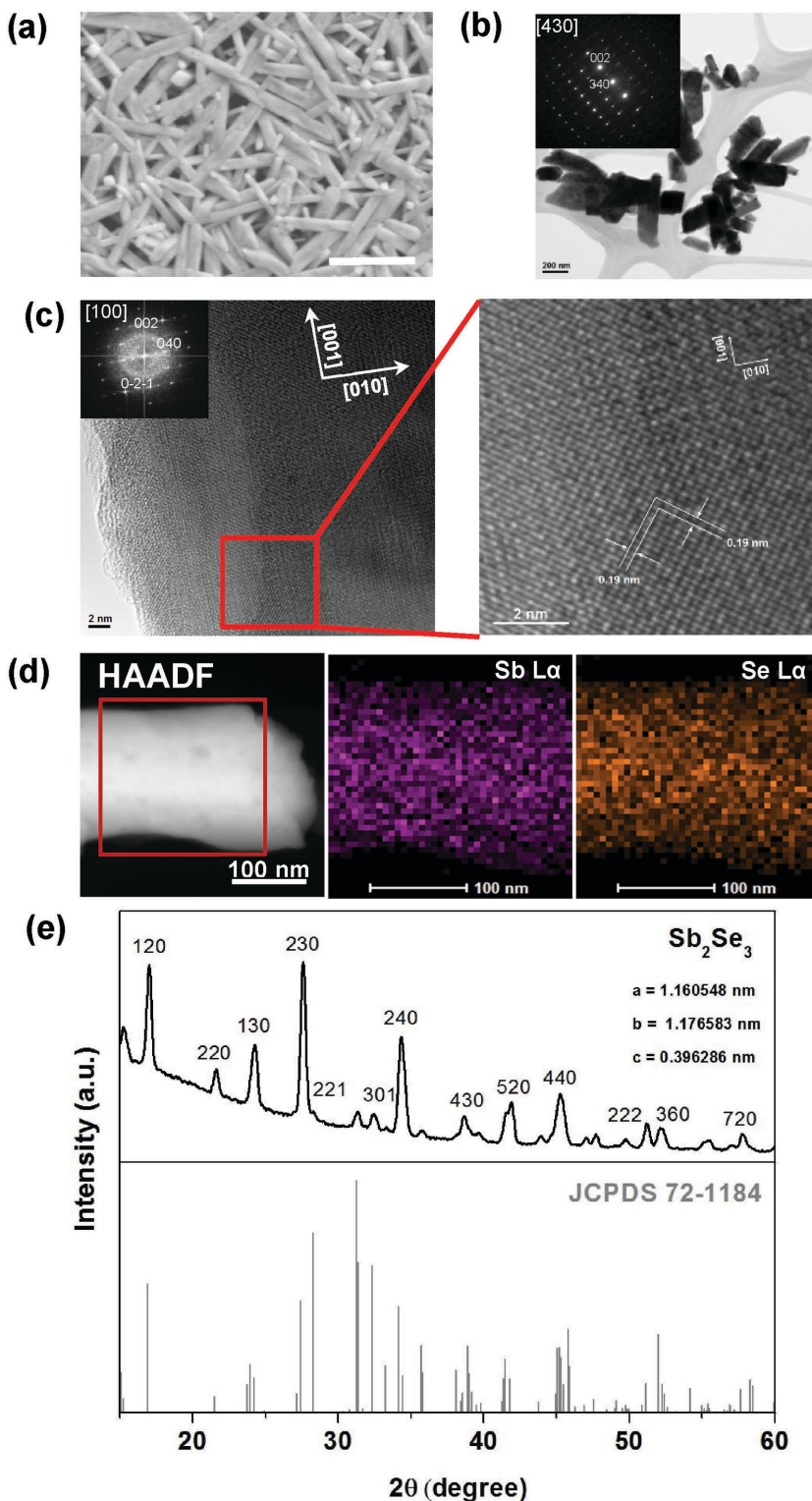


**Figure 2.** Analytical electron microscopy and XRD analysis of  $\text{Sb}_2\text{Se}_3$  NWs: a) High magnification FESEM image. The scale bar corresponds to 1  $\mu\text{m}$ . b) Bright-field (BF) TEM of  $\text{Sb}_2\text{Se}_3$  NWs with an SAED pattern in the [430] orientation (inset). c) HRTEM of a single crystalline orthorhombic NW growing along the  $\langle 001 \rangle$  direction with the corresponding FFT pattern in the [100] orientation (upper left inset). The right inset shows an enlargement of the area marked by the red box on the left showing the (022) and (0-22) lattice fringes. d) HAADF-STEM image of an  $\text{Sb}_2\text{Se}_3$  NW and corresponding Sb  $L\alpha$  and Se  $L\alpha$  X-ray maps (right insets). e) GIXRD pattern of the  $\text{Sb}_2\text{Se}_3$  NW film, the calculated lattice constants (top) and stick pattern JCPDS card, No. 72-1184 (bottom).

200 eV energy windows for both Sb  $M_{4,5}$ - and Se  $L_{2,3}$ -edges and corresponding calculated Hartree-Slater ionization cross-sections.<sup>[46]</sup> Quantification results demonstrate that the Sb/Se atomic ratio in the NWs is close to stoichiometric with excellent agreement between the employed analytical techniques (Table 1).

We further confirmed the crystal structure of the  $\text{Sb}_2\text{Se}_3$  NW films using grazing incidence X-ray diffraction (GIXRD), as shown in Figure 2e. All of the diffraction peaks can be indexed to the orthorhombic phase of  $\text{Sb}_2\text{Se}_3$  (JCPDS Card No. 72-1184) with a space group of  $Pbnm$  (62). All of the major planes were indexed, and no secondary phases were detected. Using retrieval analysis, the lattice constants are calculated as:  $a = (1.160584 \pm 0.0004)$  nm,  $b = (1.176583 \pm 0.0005)$  nm, and  $c = (0.396286 \pm 0.0002)$  nm, very close to the ideal bulk values for  $\text{Sb}_2\text{Se}_3$  ( $a = 1.162$  nm,  $b = 1.177$  nm,  $c = 0.3962$  nm), and consistent with previously reported data.<sup>[25,47,48]</sup>

X-ray photoelectron spectroscopy (XPS) measurements were further carried out to characterize the chemical state of  $\text{Sb}_2\text{Se}_3$  as well as the presence of  $\text{Sb}_2\text{O}_3$ . Figure S9 (Supporting Information) shows a high-resolution XPS spectrum for the Sb 3d core level. The binding energies located at  $(529.2 \pm 0.3)$  eV and  $(538.6 \pm 0.3)$  eV correspond to  $\text{Sb}_{5/2}$  and  $\text{Sb}_{3/2}$  and are consistent with Sb 3d core levels for  $\text{Sb}_2\text{Se}_3$ .<sup>[48]</sup> In addition, binding energies located at  $(530.5 \pm 0.3)$  eV and  $(539.9 \pm 0.3)$  eV correspond to the core levels of  $\text{Sb}_{5/2}$  and  $\text{Sb}_{3/2}$  for  $\text{Sb}_2\text{O}_3$ .<sup>[49]</sup> The storage of the films in air before the XPS measurement provides an explanation for the presence of oxide in the film.

In order to determine the transition type and the optical band gap, a transmission spectrum of the  $\text{Sb}_2\text{Se}_3$  NW thin films was recorded using UV-vis absorption spectroscopy. The band gap was estimated by extrapolating the linear region of the Tauc plots of  $(\alpha h\nu)^2$  versus  $h\nu$  to  $h\nu = 0$  (Figure 3a), where  $\alpha$  is the absorption coefficient and  $h\nu$  is the photon energy. A direct transition type with a value of  $\approx 1.12$  eV was confirmed, quite close to previously reported values,<sup>[7]</sup> as well as those measured by ellipsometry (Figure S5, Supporting Information).

We also computed the electronic band structure of bulk  $\text{Sb}_2\text{Se}_3$  using density functional theory and found good agreement with the measured band gap of the deposited NWs. The calculated minimum gap of 0.90 eV for  $\text{Sb}_2\text{Se}_3$  was found to be indirect, and the direct gap was 1.05 eV, a difference of 0.15 eV from the indirect gap, making the direct and indirect transitions almost

**Table 1.** Quantitative EDXS and EELS analyses of  $\text{Sb}_2\text{Se}_3$  NWs.

Technique	Accelerating voltage [kV]	Sb/Se atomic ratio, $\pm 2\sigma$ at the 95% confidence limit
EDXS-STEM Cliff-Lorimer thin film ratio method with calculated k-factors for the Sb $K\alpha$ and the Se $K\alpha$ peaks and absorption (mass-thickness) correction	300	$0.65 \pm 0.09$
EELS thin film ratio method with 200 eV integration windows for the Sb $M_{4,5}$ - and the Se $L_{2,3}$ -edges	300	$0.65 \pm 0.04$

degenerate, as previously reported<sup>[50]</sup> (Figure 3b). Furthermore, the band structure of  $\text{Sb}_2\text{Se}_3$  exhibits several transitions between the valence band and the conduction band with comparable energy to the fundamental indirect-gap energy, suggesting that  $\text{Sb}_2\text{Se}_3$  can be considered a direct gap semiconductor for all practical applications. The states at the valence band edge are predominantly associated with Se p-orbitals and those at the conduction band edge are dominated by the Sb p-orbitals. The density of states (DOS) for bulk  $\text{Sb}_2\text{Se}_3$  shown in Figure 3c agrees well with earlier work.<sup>[24]</sup> The close agreement in the band gap of bulk  $\text{Sb}_2\text{Se}_3$  and solution-deposited  $\text{Sb}_2\text{Se}_3$  NWs indicates surface and quantum confinement effects play little

role in the electronic structure of the NWs. In addition, Raman spectroscopy performed on  $\text{Sb}_2\text{Se}_3$  NWs revealed two Raman peaks centered at  $(190 \pm 0.3)$  and  $(253 \pm 0.3) \text{ cm}^{-1}$  which represent the hetero-polar Sb–Se and nonpolar Sb–Sb vibrations<sup>[25]</sup> (Figure 3d). The additional minor peaks located at  $\approx 160$  and  $\approx 212 \text{ cm}^{-1}$  can potentially be attributed to the oxidation of the film or  $\text{Sb}_2\text{O}_3$ .<sup>[51]</sup> Raman mapping also shows the uniformity of those peaks (Figure S6, Supporting Information).

After establishing the crystal structure and optical properties of the molecular-ink-based  $\text{Sb}_2\text{Se}_3$  NWs, we fabricated flexible photoconductive PDs by depositing interdigitated Au/Ti/Au electrodes via electron beam evaporation on the NW-polyimide substrates (inset of Figure 4a). Figure 4a shows a current–voltage ( $I$ – $V$ ) characteristic curve for an  $\text{Sb}_2\text{Se}_3$  NW PD measured in the dark and under 870 nm illumination. At an applied bias ranging from  $-30$  to  $30 \text{ V}$  with a very low illumination intensity of  $\approx 6.4 \mu\text{W}$ , the change in slope of the  $I$ – $V$  curve indicates a strong photoresponse, and the linear  $I$ – $V$  curve evinces the Ohmic nature of the contact between the metal electrodes and NWs.

The temporal response of the PD under pulsed 365 nm illumination ( $30 \text{ mW cm}^{-2}$ , 20 and 90 s pulse widths) and 10 V bias is presented in Figure 4b. Both shorter (20 s pulse width) and longer (90 s pulse width) periods of modulation were performed to demonstrate the photocurrent stability. The PD photocurrent is reproducible and stable with two distinct states: a “low” current state in the dark and a “high” current state under illumination with an on/off ratio of  $\approx 22$ . The characteristic rise time ( $t_r$ ) for the photocurrent to increase from 10% to 90% of

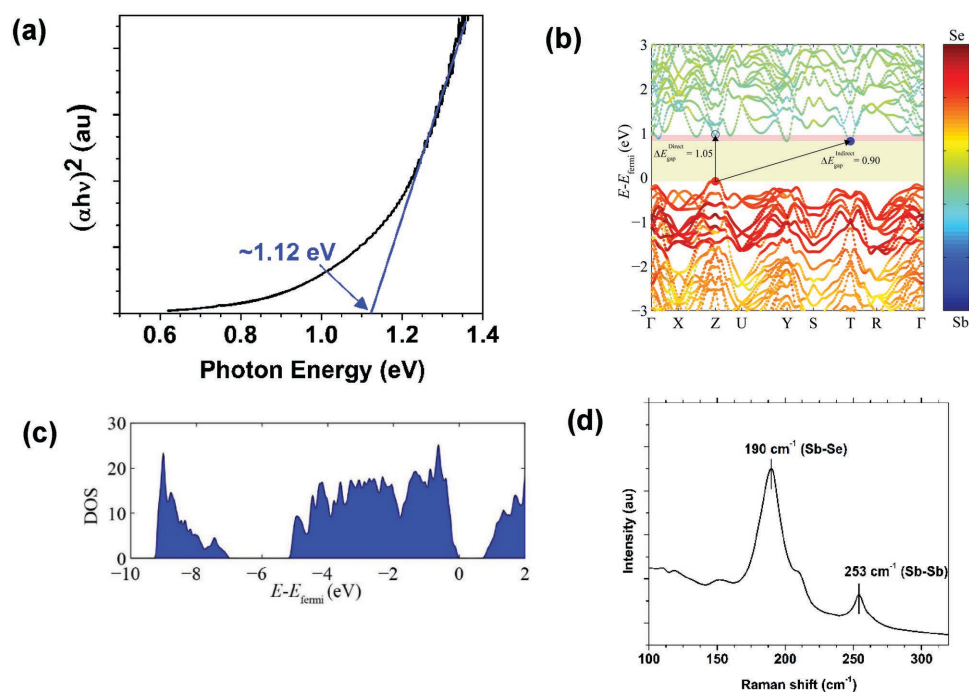


**Figure 3.** Optical properties of  $\text{Sb}_2\text{Se}_3$ : a) Tauc plot used to estimate the band gap ( $\approx 1.12 \text{ eV}$ ) from a linear interpolation. b) Electronic band structure of bulk  $\text{Sb}_2\text{Se}_3$  computed using DFT simulations.  $\text{Sb}_2\text{Se}_3$  has an indirect band gap,  $\Delta E_{\text{gap}}^{\text{indirect}}$ , of 0.90 eV and a direct band gap,  $\Delta E_{\text{gap}}^{\text{direct}}$ , of 1.05 eV. The valence band maxima and conduction band minima are marked with red and blue circles, respectively. The symbol sizes and colors denote the weights of the Sb or Se contributions to the bands. The valence band maximum is set to zero energy. c) The calculated DOS versus  $E - E_{\text{fermi}}$  in eV. d) Raman spectrum showing the heteropolar Sb–Se and nonpolar Sb–Sb vibrations.

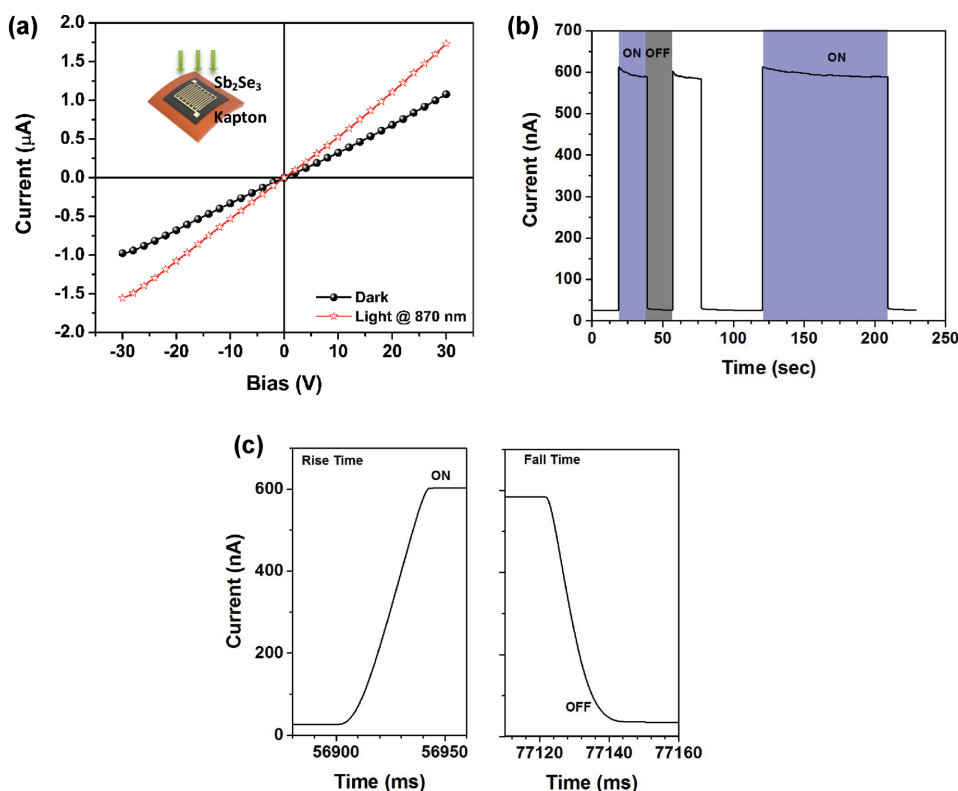


**Figure 4.** Photoconductive device properties: a)  $I$ - $V$  curves measured in the dark and under 870 nm illumination with a light intensity of  $6.4 \mu\text{W}$ . The inset shows a schematic of the fabricated PD with interdigitated electrodes. b) Temporal photocurrent response under 365 nm pulsed light ( $\approx 30 \text{ mW cm}^{-2}$ ) with periods of 20 and 90 s (to demonstrate stability) at an applied bias of 10 V. c) Zoomed-in temporal photocurrent response illustrating the rise ( $24 \pm 2 \text{ ms}$ ) and decay ( $9 \pm 2 \text{ ms}$ ) times measured in one period of modulation.

its maximum value is  $(24 \pm 2) \text{ ms}$ , and the decay time ( $t_d$ ) for the photocurrent to decrease from 90% to 10% of the peak value is  $(9 \pm 2) \text{ ms}$  (as illustrated in Figure 4c). This temporal response is significantly faster than in previous  $\text{Sb}_2\text{Se}_3$ -based PD demonstrations with both response and recovery times that are two orders of magnitude smaller than previously reported values ( $24$  and  $9 \text{ ms}$  vs  $0.18$  and  $0.20 \text{ s}$ ).<sup>[32,44]</sup>

Device photoresponse is generally governed by complex processes such as carrier generation, trapping, and recombination. Due to the nanostructured nature of the PD active layer, abundant grain boundaries (or junction barriers) are expected to be present in the NW film. This type of defect is generally associated with the formation of deep traps leading to slow temporal response. Instead, the NW film measured here exhibits fast decay and recovery times. This can potentially be attributed to the high-quality crystalline nature of the materials, which leads to efficient optical absorption and photocarrier generation under illumination. The increased carrier density reduces the junction barrier height between the adjacent NWs, and such light-induced barrier height modulation could lead to the fast response time. Additionally, the large surface-to-volume ratio of the NWs is likely associated with a high density of surface-associated dangling bonds/defects. Thus, when the light is turned off, the carriers can recombine quickly, resulting in short decay times.

We also obtained the spectral response of the PD by scaling the measured photocurrent to that of a calibrated Si PD. Given

nominally identical illumination conditions under applied bias, this measurement can be used to extract the external quantum efficiency (EQE) of the device. Figure 5a (top) is a contour plot of the device EQE, which increases monotonically with the applied bias. It can be seen that the applied bias influences the on/off ratio of the PDs, which is related to the bias dependence of the exciton dissociation and the background current. The EQE at 30 V reaches a maximum of  $\approx 35\%$  in the NIR (at 1.43 eV) and  $\approx 51\%$  in the UV (at 4.13 eV); however, it remains lower in the visible regime.

In order to investigate the source of the partial visible transparency present in the EQE spectra, we ran a series of finite-difference time-domain (FDTD) optical simulations of single nanowires and nanowire arrays. The nanowires in the arrays were randomly oriented and modeled as cylinders with a uniform distribution of 250 nm in diameter and 900 nm in length (Figure S7c, Supporting Information), based on the SEM measurements of the as-grown samples. Their refractive indices were determined from ellipsometry measurements, and absorption and reflection spectra (Figure S7a,b,d, Supporting Information) as well as spatial electric field data were obtained for nanowire arrays, planar  $\text{Sb}_2\text{Se}_3$  control films of comparable total thickness, and single nanowires.

The FDTD single NW absorption results qualitatively reproduce the observed dip in the visible region of the EQE spectra (Figure S7d, Supporting Information), while the planar device absorption has less of a spectral discrepancy across the same

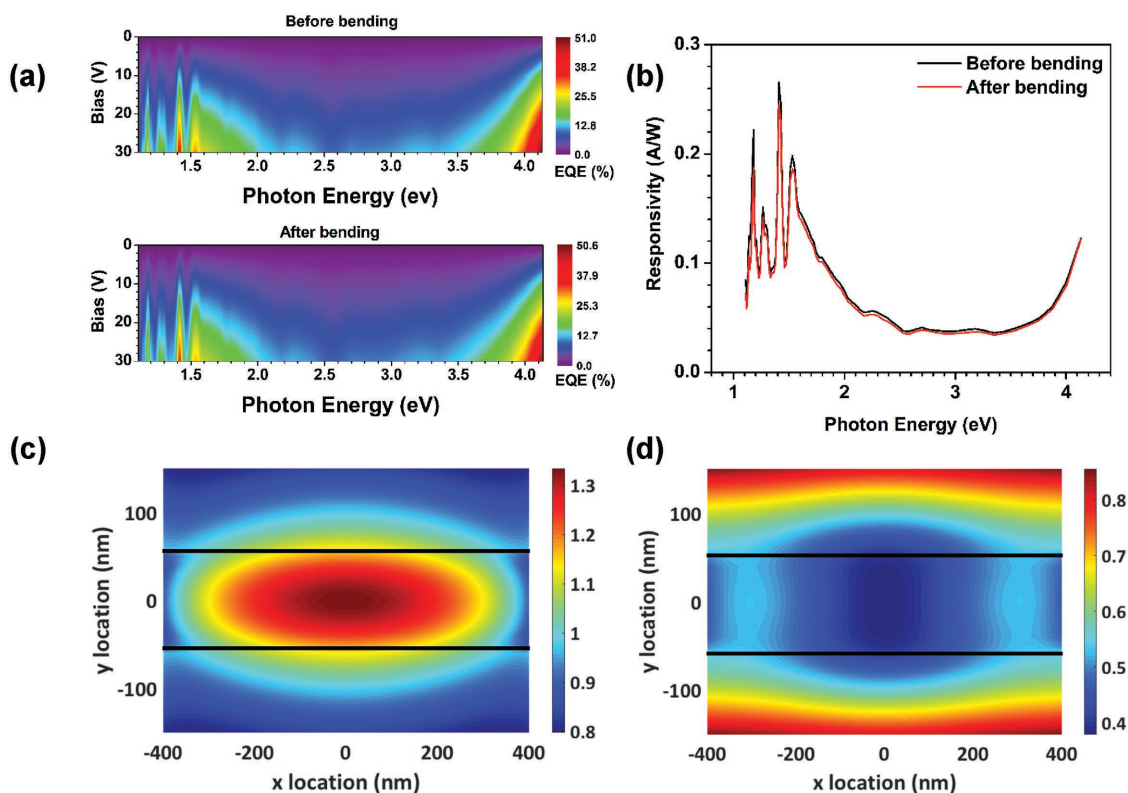


**Figure 5.** Figures of merit of the PDs: a) EQE data as a function of applied bias: as-made device (before bending: top) and after 40 bending cycles (after bending: bottom) over a radius of curvature of 1 cm. b) Representative spectral responsivity of the same device at an applied bias of 30 V. The mechanical robustness of the device is evident even after 40 bending cycles. Calculated FDTD normalized electric field intensity for an average-sized single  $\text{Sb}_2\text{Se}_3$  nanowire at the plane normal to the incident illumination (s-polarized source) at c)  $\lambda = 1100$  nm and d)  $\lambda = 650$  nm. The presence of a waveguide mode in (c) versus the absence of a confined mode within the NW in (d) demonstrates a possible explanation for the enhanced NIR performance seen in (a) and (b).

range (Figure S7a, Supporting Information). The single nanowire results give a potential explanation for this phenomenon: in the visible region, the most common size of nanowire does not support a waveguide mode; however, in the NIR, the nanowire supports a strong mode, leading to enhanced in-coupling and waveguiding in the nanowire array. Nanowire spatial electric field profiles are plotted in Figure 5c,d for 1100 and 650 nm illuminations, respectively. The absorption spectra in Figure S7a (Supporting Information) also display resonance peaks in the NIR regime similar to peaks observed in the device EQE and spectral responsivity (Figure 5a,b respectively). Additionally, Figure S7e (Supporting Information) shows the reflection spectrum of the fabricated  $\text{Sb}_2\text{Se}_3$  nanowire film without electrodes. The small pitch of the interdigitated electrodes (IDEs; 100  $\mu\text{m}$ ) leads to a shadowing effect that results in the loss of a fraction of the incoming light ( $\approx 35\%$ ). This shadowing could be reduced in future systems by replacing the opaque electrodes with thinner metals or transparent conductive oxides and optimizing their fill fraction.

These results imply that the spectral responsivity of the PDs could be tuned by changing the size of the nanowires in the array. The nanowire size is controlled by relative precursor concentration during growth and post-annealing conditions. This tuning knob could be used to enable enhanced broadband performance of the molecular-ink based PDs. Additionally,

controlling the nanowire size would allow for the realization of spectrally selective detection by enhancing or suppressing performance in specific spectral bands.

Mechanical stability is critical for practical applications of flexible optoelectronics. We measured the device photocurrent after 40 bending cycles over a radius of curvature of  $\approx 10$  mm. As shown in Figure 5a (bottom), there is no significant change in the EQE after many bending cycles, demonstrating the robustness of these PDs.

The responsivity ( $R_\lambda$ ), another critical measure of PD performance, has also been calculated using Equation (1)

$$R_\lambda = \frac{I_{\text{light}}}{P_0} \quad (1)$$

where  $I_{\text{light}}$  is the device photocurrent under UV illumination, and  $P_0$  is the light intensity. The calculated responsivities of the devices at 30 V bias are shown in Figure 5b before and after bending. The maximum responsivity reaches  $\approx 0.27$   $\text{A W}^{-1}$  at 880 nm and experiences only a slight decrease to  $\approx 0.25$   $\text{A W}^{-1}$  after 40 bending cycles, comparable with other broadband PD technologies.

The figures of merit for these molecular-ink-based PDs could be further improved by optimizing the processing conditions and tuning the gap between the two IDEs to optimize the

metallized area. Optically, tuning the nanowire size could target waveguiding and enhanced performance in the visible regime. One could also employ alternative light trapping and optical enhancement schemes such as integration of nanoscale plasmonic structures to improve in-coupling and benefit from local field enhancements.<sup>[52]</sup> Exploring these approaches is beyond the scope of this paper.

A facile, scalable, template-free route was developed to grow  $\text{Sb}_2\text{Se}_3$  nanostructures directly on flexible substrates. Our molecular ink was prepared from elemental antimony and selenium dissolved in amine/thiol solvents and deposited at room temperature, employing a chemical method that should be extendable to other technologies. Compositional analysis and structural characterization of the resulting nanowires depict chemically pure, high-quality single-crystalline nanostructures with near stoichiometric composition. The fabricated PDs exhibit fast response and excellent figures of merit. Manipulating the nanowire size is an additional tuning knob that could be used to enhance the broadband performance and build spectrally selective optoelectronics. The negligible change in photoresponse after multiple bending cycles is evidence of excellent mechanical stability which makes the molecular inks a promising platform for low-cost, flexible and portable broadband photon detection, photoelectronic switches, and other optoelectronic devices.

## Experimental Section

**Growth of  $\text{Sb}_2\text{Se}_3$  Nanostructures:** In a typical synthesis, 2.5 mmol (304 mg) antimony (Alfa Aesar, 99.5+%) and 7.5 mmol (590 mg) selenium (Alfa Aesar, 99.999%) were weighed in a 20 mL vial and transferred to a nitrogen-filled globe box (MBraun, <0.1 ppm  $\text{O}_2$  and <0.1 ppm  $\text{H}_2\text{O}$ ). Then, 5.0 mL EDA (Alfa Aesar, 99+%) and 1.5 mL of ME (Alfa Aesar, 98+%) were added to the vial. The solution was stirred for several days until complete dissolution of the constituent elements occurred, resulting in a dark orange color. To obtain nanograin-like morphology rather than nanowires (Figure S1a, Supporting information), the selenium concentration was reduced to 4 mmol (316 mg), resulting in a final solution of light orange color (not shown).

**Thin Film Fabrication and Metallization:** The obtained  $\text{Sb}_2\text{Se}_3$  ink was spin-cast onto a polyimide film (Dupont, Kapton HN) at 1500 rpm for 40 s in a nitrogen glove box, and the deposited thin films were annealed at 350 °C for 5 min inside the glove box. We speculate that the ink as-synthesized is a polymeric complex in an organometallic compound solution, which converts to  $\text{Sb}_2\text{Se}_3$  after thermal annealing. The antimony can bond with thiols (–SH) and amines (– $\text{NH}_2$ ), forming long chain when added to the solvents. Selenium can also form S–Se bonds or Se–Se rings in the solution. The polymeric chains possibly break at random locations when this complex polymeric film is annealed at high temperature, and this results in nanowire formation. Additionally, we speculate that the functional chains of the polyimide substrate may also play a critical role for wire formation. Subsequently, the substrates were taken out of the glove box and stored in air. IDEs with metal contacts of Au/Ti/Au (20/90/20 nm) were evaporated at a rate of about (0.5–1) Å  $\text{s}^{-1}$  through a shadow mask using electron-beam evaporation. Both the width and the spacing between the adjacent electrodes (pitch) were fixed at 100  $\mu\text{m}$ . The device area was about 16  $\text{mm}^2$ , and four devices were patterned on each 15 × 15  $\text{mm}^2$  polyimide substrate.

**Characterization:** The microstructure and composition of the materials were examined using a JEOL JSM-7100 FLV variable vacuum FESEM equipped with an Oxford Instruments 80  $\text{mm}^2$  X-Max silicon-drift energy dispersive X-ray detector (EDXS SDD) and AZtec integrated microanalysis system. Scanning and transmission electron microscopy

(S/TEM) imaging in various modes, SAED, EEL, and EDXS spectroscopic analyses of the  $\text{Sb}_2\text{Se}_3$  nanostructures were performed in a Schottky field-emission FEI Titan 80–300 analytical S/TEM with a point-to-point resolution of 0.19 nm and information limit below 0.1 nm equipped with S-TWIN objective lenses and operating at 300 kV accelerating voltage. For high spatial resolution nanoanalysis in the STEM mode using a 0.2 nm diameter probe, the instrument was equipped with a Fischione 3000 model high-angle annular dark-field (HAADF) detector, FEI BF- and ADF-STEM detectors, a Gatan Enfina electron spectrometer, and a 30  $\text{mm}^2$  EDAX Si/Li EDX detector with a 0.13 srad acceptance angle. To ensure optimal counting rates, the specimens were tilted at an angle of 15° toward the EDX detector. Crystallinity of the deposited films was characterized using a Rigaku SmartLab XRD system. JCPDS Card No. 72–1184 was used as it matched closely with our  $\text{Sb}_2\text{Se}_3$  XRD data having an orthorhombic phase with a space group of  $P_{bnm}$  as compared to other JCPDS cards. An integrated HORIBA Jobin Yvon LabRAM 800HR bench-top system was used for Raman spectroscopy using a 532 nm laser (Laser Quantum DPSS) with a spot size of  $\approx 1 \mu\text{m}$ .

XPS was used to validate the chemical composition of the NW film, and the spectra were collected in a Kratos Axis Ultra DLD spectrometer with an Al K $\alpha$  monochromatic X-ray source and an analyzer with 0.1 eV energy steps and 20 eV pass energy for high-resolution scans. The XPS spectra were energy calibrated to the adventitious C 1s binding energy at (284.5 ± 0.3) eV.

UV–vis–NIR absorption spectroscopy (Lambda 950 Perkin Elmer) was used to determine optical band gaps, extracted by employing Tauc plots. Vacuum ultraviolet variable angle ellipsometry (VUV-VASE) measurements were also performed to determine the dielectric functions of the films from which the band gaps were extracted.

PD devices were characterized by current–voltage ( $I$ – $V$ ) and EQE measurements using a spectrally filtered light source, and the system was calibrated using an NIST-calibrated silicon photodiode. A total uncertainty of ± 5% (fractional) is associated with the measured EQE under AM1.5 illumination. For transient response measurements, PD devices were illuminated using a Panasonic Aicure UJ30 system equipped with a 365 nm UV light emitting diode, and currents were monitored with and without UV light using an Agilent B1500A semiconductor device parameter analyzer.

**Simulation:** Density functional theory (DFT) simulations used the projector augmented wave method as implemented in the plane-wave code VASP.<sup>[53–57]</sup> For the structural relaxations, the optB88-vdW functional was employed, which includes van der Waals interactions.<sup>[58,59]</sup> Employing a cutoff energy of 400 eV and a k-point mesh density of 80 per Å<sup>−1</sup>, the structure of the  $\text{Sb}_2\text{Se}_3$  was optimized until forces and in-plane stresses were below 0.005 eV Å<sup>−1</sup> and 0.001 GPa, respectively. The lattice constants of  $\text{Sb}_2\text{Se}_3$  were found to be  $a = 1.2055 \text{ nm}$ ,  $b = 1.1607 \text{ nm}$ , and  $c = 0.4042 \text{ nm}$ , within 2% of the experimentally measured lattice parameters from GIXRD. A high k-point mesh density of 120 Å<sup>−1</sup> was used for the standard DFT electronic structure determination under the generalized gradient approximation. Using a k-point mesh density of 20 Å<sup>−1</sup>, the more expensive functional HSE06<sup>[60,61]</sup> resulted in a 0.15 eV difference between the indirect and direct gaps. While the electronic structure of  $\text{Sb}_2\text{Se}_3$  has been previously reported, the weak van der Waals interactions are not accounted for in the existing literature.<sup>[24,50,62–66]</sup> There is a large variation in the theoretically predicted band gaps, ranging from 0.75–1.14 eV (indirect gap) and 0.78–1.27 eV (direct gap),<sup>[50,63–66]</sup> and the existing DFT-based and GW-based simulations report only a small fraction of the paths along the high-symmetry k-points.<sup>[50,62,64,65]</sup>

FDTD calculations were performed using commercial software (Lumerical, Inc.). A broadband plane wave source spanning a wavelength range of 300–2000 nm was used as the excitation source. The nanowires were modeled as cylinders with a uniform distribution of 250 nm in diameter and 900 nm in length on a polyimide substrate. The nanowire array was composed of randomly oriented cylinders in all three axes with an angular distribution from 0° to 180°. Refractive index data ( $n$  and  $k$ ) for  $\text{Sb}_2\text{Se}_3$  were obtained from ellipsometry measurements. Monitors were placed behind the incident source, in front of, and beyond the structure to obtain absorption, reflection, and spatial electrical field data.

## Supporting Information

Supporting Information is available from the Wiley Online Library or from the author.

## Acknowledgements

M.R.H. acknowledges the financial support of NSF grant No. 203146. A.K.S. is funded by the Professional Research Experience Postdoctoral Fellowship under award No. 70NANB11H012. This research used computational resources provided by the Texas Advanced Computing Center under Contracts TG-DMR050028N, TG-DMR140143, and TG-DMR150006. This work used the Extreme Science and Engineering Discovery Environment (XSEDE), which was supported by National Science Foundation grant number ACI-1053575. The devices were fabricated in the Nanofab of the NIST Center for Nanoscale Science and Technology (CNST). The authors are grateful to Dr. Nikolai Zhitenev and Dr. Veronika Szalai of CNST, NIST for their valuable help with device fabrication and Raman spectroscopy measurements, respectively. Certain commercial equipment, instruments, or materials are identified in this paper in order to specify the experimental procedure adequately. Such identification is not intended to imply recommendation or endorsement by the National Institute of Standards and Technology (NIST), nor is it intended to imply that the materials or equipment identified are necessarily the best available for the purpose.

Received: May 3, 2016

Revised: July 11, 2016

Published online:

- [1] H. E. Katz, A. J. Lovinger, J. Johnson, C. Kloc, T. Siegrist, W. Li, Y.-Y. Lin, A. Dodabalapur, *Nature* **2000**, 404, 478.
- [2] C. R. Kagan, D. B. Mitzi, C. D. Dimitrakopoulos, *Science* **1999**, 286, 945.
- [3] X. Duan, C. Niu, V. Sahi, J. Chen, J. W. Parce, S. Empedocles, J. L. Goldman, *Nature* **2003**, 425, 274.
- [4] H. Sirringhaus, T. Kawase, R. H. Friend, T. Shimoda, M. Inbasekaran, W. Wu, E. P. Woo, *Science* **2000**, 290, 2123.
- [5] B. A. Ridley, B. Nivi, J. M. Jacobson, *Science* **1999**, 286, 746.
- [6] D. B. Mitzi, L. L. Kosbar, C. E. Murray, M. Copel, A. Afzali, *Nature* **2004**, 428, 299.
- [7] Y. Zhou, M. Leng, Z. Xia, J. Zhong, H. Song, X. Liu, B. Yang, J. Zhang, J. Chen, K. Zhou, J. Han, Y. Cheng, J. Tang, *Adv. Energy Mater.* **2014**, 4, 1301846.
- [8] D. B. Mitzi, M. Copel, S. J. Chey, *Adv. Mater.* **2005**, 17, 1285.
- [9] F. Zhang, C. Di, N. Berdunov, Y. Hu, Y. Hu, X. Gao, Q. Meng, H. Sirringhaus, D. Zhu, *Adv. Mater.* **2013**, 25, 1401.
- [10] A. R. Brown, A. Pomp, C. M. Hart, D. M. de Leeuw, *Science* **1995**, 270, 972.
- [11] H. E. A. Huitema, G. H. Gelinck, J. B. P. H. van der Putten, K. E. Kuijk, C. M. Hart, E. Cantatore, P. T. Herwig, A. J. J. M. van Breemen, D. M. de Leeuw, *Nature* **2001**, 414, 599.
- [12] F. Garnier, R. Hajlaoui, A. Yassar, P. Srivastava, *Science* **1994**, 265, 1684.
- [13] G. H. Gelinck, H. E. A. Huitema, E. van Veenendaal, E. Cantatore, L. Schrijnemakers, J. B. P. H. van der Putten, T. C. T. Geuns, M. Beenhakkers, J. B. Giesbers, B.-H. Huisman, E. J. Meijer, E. M. Benito, F. J. Touwslager, A. W. Marsman, B. J. E. van Rens, D. M. de Leeuw, *Nat. Mater.* **2004**, 3, 106.
- [14] Y. Sun, G. C. Welch, W. L. Leong, C. J. Takacs, G. C. Bazan, A. J. Heeger, *Nat. Mater.* **2012**, 11, 44.
- [15] D. B. Mitzi, *J. Mater. Chem.* **2004**, 14, 2355.
- [16] J.-S. Lee, M. V. Kovalenko, J. Huang, D. S. Chung, D. V. Talapin, *Nat. Nanotechnol.* **2011**, 6, 348.
- [17] A. M. Smith, S. Nie, *Acc. Chem. Res.* **2010**, 43, 190.
- [18] P. K. Nair, M. T. S. Nair, V. M. García, O. L. Arenas, A. C. Peña, I. T. Ayala, O. Gomezdaza, A. Sánchez, J. Campos, H. Hu, R. Suárez, M. E. Rincón, *Sol. Energy Mater. Sol. Cells* **1998**, 52, 313.
- [19] O. Niitsoo, S. K. Sarkar, C. Pejoux, S. Rühle, D. Cahen, G. Hodes, *J. Photochem. Photobiol., A* **2006**, 181, 306.
- [20] H. Lee, M. Wang, P. Chen, D. R. Gamelin, S. M. Zakeeruddin, M. Grätzel, M. K. Nazeeruddin, *Nano Lett.* **2009**, 9, 4221.
- [21] H. J. Lee, J. Bang, J. Park, S. Kim, S.-M. Park, *Chem. Mater.* **2010**, 22, 5636.
- [22] S. A. Studenikin, N. Golego, M. Cocivera, *J. Appl. Phys.* **1998**, 84, 2287.
- [23] F. Paraguay, D. W. Estrada, L. D. R. Acosta, N. E. Andrade, M. Miki-Yoshida, *Thin Solid Films* **1999**, 350, 192.
- [24] Y. Zhou, L. Wang, S. Chen, S. Qin, X. Liu, J. Chen, D.-J. Xue, M. Luo, Y. Cao, Y. Cheng, E. H. Sargent, J. Tang, *Nat. Photonics* **2015**, 9, 409.
- [25] Y.-Q. Liu, M. Zhang, F.-X. Wang, G.-B. Pan, *J. Mater. Chem. C* **2013**, 2, 240.
- [26] D. T. Morelli, V. Jovovic, J. P. Heremans, *Phys. Rev. Lett.* **2008**, 101, 035901.
- [27] G. Domingo, R. S. Itoga, C. R. Kannewurf, *Phys. Rev.* **1966**, 143, 536.
- [28] Y. C. Choi, T. N. Mandal, W. S. Yang, Y. H. Lee, S. H. Im, J. H. Noh, S. I. Seok, *Angew. Chem., Int. Ed.* **2014**, 53, 1329.
- [29] Y. Kim, A. DiVenere, G. K. L. Wong, J. B. Ketterson, S. Cho, J. R. Meyer, *J. Appl. Phys.* **2002**, 91, 715.
- [30] A. Boulouz, S. Chakraborty, A. Giani, F. P. Delannoy, A. Boyer, J. Schumann, *J. Appl. Phys.* **2001**, 89, 5009.
- [31] R. Huang, J. Zhang, F. Wei, L. Shi, T. Kong, G. Cheng, *Adv. Funct. Mater.* **2014**, 24, 3581.
- [32] T. Zhai, M. Ye, L. Li, X. Fang, M. Liao, Y. Li, Y. Koide, Y. Bando, D. Golberg, *Adv. Mater.* **2010**, 22, 4530.
- [33] D. Choi, Y. Jang, J. Lee, G. H. Jeong, D. Whang, S. W. Hwang, K.-S. Cho, S.-W. Kim, *Sci. Rep.* **2014**, 4, 6714.
- [34] M. Wuttig, N. Yamada, *Nat. Mater.* **2007**, 6, 824.
- [35] R. B. Yang, J. Bachmann, E. Pippel, A. Berger, J. Woltersdorf, U. Gösele, K. Nielsch, *Adv. Mater.* **2009**, 21, 3170.
- [36] F. Verger, V. Nazabal, F. Colas, P. Nêmec, C. Cardinaud, E. Baudet, R. Chahal, E. Rinnert, K. Boukerma, I. Peron, S. Deputier, M. Guilloux-Viry, J. P. Guin, H. Lhermite, A. Moreac, C. Compère, B. Bureau, *Opt. Mater. Express* **2013**, 3, 2112.
- [37] M. Luo, M. Leng, X. Liu, J. Chen, C. Chen, S. Qin, J. Tang, *Appl. Phys. Lett.* **2014**, 104, 173904.
- [38] N. V. Tarakina, S. Schreyeck, T. Borzenko, C. Schumacher, G. Karczewski, K. Brunner, C. Gould, H. Buhmann, L. W. Molenkamp, *Cryst. Growth Des.* **2012**, 12, 1913.
- [39] D. H. Webber, R. L. Brutchey, *J. Am. Chem. Soc.* **2013**, 135, 15722.
- [40] T. K. Todorov, K. B. Reuter, D. B. Mitzi, *Adv. Mater.* **2010**, 22, E156.
- [41] C. L. McCarthy, D. H. Webber, E. C. Schueller, R. L. Brutchey, *Angew. Chem. Int. Ed.* **2015**, 54, 8378.
- [42] D. H. Webber, J. J. Buckley, P. D. Antunez, R. L. Brutchey, *Chem. Sci.* **2014**, 5, 2498.
- [43] J. Ma, Y. Wang, Y. Wang, Q. Chen, J. Lian, W. Zheng, *J. Phys. Chem. C* **2009**, 113, 13588.
- [44] G. Chen, W. Wang, C. Wang, T. Ding, Q. Yang, *Adv. Sci.* **2015**, 2, 1570040.
- [45] G. Cliff, G. W. Lorimer, *J. Microsc.* **1975**, 103, 203.
- [46] R. F. Egerton, *Electron Energy-Loss Spectroscopy in the Electron Microscope*, Springer Science & Business Media, New York, USA **2011**.
- [47] N. Maiti, S. H. Im, Y. H. Lee, C.-H. Kim, S. I. Seok, *CrystEngComm* **2011**, 13, 3767.

- [48] X. Liu, J. Chen, M. Luo, M. Leng, Z. Xia, Y. Zhou, S. Qin, D.-J. Xue, L. Lv, H. Huang, D. Niu, J. Tang, *ACS Appl. Mater. Interfaces* **2014**, *6*, 10687.
- [49] T. Birchall, J. A. Connor, L. H. Hillier, *J. Chem. Soc., Dalton Trans.* **1975**, *20*, , 2003.
- [50] R. Vadapoo, S. Krishnan, H. Yilmaz, C. Marin, *Phys. Status Solidi B* **2011**, *248*, 700.
- [51] Z. Deng, F. Tang, D. Chen, X. Meng, L. Cao, B. Zou, *J. Phys. Chem. B* **2006**, *110*, 18225.
- [52] P. Berini, *Laser Photonics Rev.* **2014**, *8*, 197.
- [53] G. Kresse, J. Furthmüller, *Phys. Rev. B* **1996**, *54*, 11169.
- [54] G. Kresse, J. Hafner, *Phys. Rev. B* **1993**, *47*, 558.
- [55] G. Kresse, J. Hafner, *Phys. Rev. B* **1994**, *49*, 14251.
- [56] G. Kresse, J. Furthmüller, *Comput. Mater. Sci.* **1996**, *6*, 15.
- [57] J. Klimeš, D. R. Bowler, A. Michaelides, *Phys. Rev. B* **2011**, *83*, 195131.
- [58] M. Dion, H. Rydberg, E. Schröder, D. C. Langreth, B. I. Lundqvist, *Phys. Rev. Lett.* **2004**, *92*, 246401.
- [59] G. Román-Pérez, J. M. Soler, *Phys. Rev. Lett.* **2009**, *103*, 096102.
- [60] J. Heyd, J. E. Peralta, G. E. Scuseria, R. L. Martin, *J. Chem. Phys.* **2005**, *123*, 174101.
- [61] J. Heyd, G. E. Scuseria, M. Ernzerhof, *J. Chem. Phys.* **2003**, *118*, 8207.
- [62] V. L. Deringer, R. P. Stoffel, M. Wuttig, R. Dronskowski, *Chem. Sci.* **2015**, *6*, 5255.
- [63] J. J. Carey, J. P. Allen, D. O. Scanlon, G. W. Watson, *J. Solid State Chem.* **2014**, *213*, 116.
- [64] M. R. Filip, C. E. Patrick, F. Giustino, *Phys. Rev. B* **2013**, *87*, 205125.
- [65] H. Koc, A. M. Mamedov, E. Deligoz, H. Ozisik, *Solid State Sci.* **2012**, *14*, 1211.
- [66] R. Caracas, X. Gonze, *Phys. Chem. Miner.* **2005**, *32*, 295.